Tomas Bata University in Zlín
Library

Laser-synthesized Ag/TiO nanoparticles to integrate catalytic pollutant degradation and antifouling enhancement in nanofibrous membranes for oil–water separation

Citation

DOI

Permanent link

TBU Publications
Repository of TBU Publications
publikace.k.utb.cz

Laser-synthesized Ag/TiO nanoparticles to integrate catalytic pollutant degradation and antifouling enhancement in nanofibrous membranes for oil-water separation

David Ettel[a], Ondřej Havelka[a], Selingul Isik[b], Daniele Silvestri[a], Stanisław Wacławek[a], Michal Urbánek[c], Vinod V.T. Padil[a], Miroslav Černík[a], Fatma Yalcinkaya[a], Rafael Torres-Mendieta[a,*]

[a]Institute for Nanomaterials, Advanced Technologies and Innovation, Technical University of Liberec, Studentská 1402/2, 461 17 Liberec, Czech Republic

[b]Faculty of Textile, Technical University of Liberec, Studentská 1402/2, 461 17 Liberec, Czech Republic

[c]Centre of Polymer Systems, University Institute, Tomas Bata University in Zlín, Trida T. Bati 5678, 760 01, Zlín, Czech Republic

[*]Corresponding author: E-mail address: Rafael.Torres@tul.cz (R. Torres-Mendieta).

ABSTRACT

In the current study, we explore the use of an eco-friendly laser-based methodology to fabricate Ag/TiO nanoparticles (NPs) with a highly controlled chemical composition, which serve to decorate the surface of Polyvinylidenefluoride (PVDF) nanofibrous membranes. Since these NPs can enhance the membranes' oil-water separation performance and independently act as catalysts with the ability to purify water, we studied the samples' separation capacity and, in parallel, the NPs pollutant degradation ability. Our findings evidence that membranes decoration by NPs with medium size (6.6 ± 2.2) nm, element composition 93.8 wt% Ti and 6.2 wt% Ag, where Ag locates in the surface, lead to a membranes' loading of $1.31 \cdot 10^{11}$ particles/cm^2 or 0.13 µg/cm^2. Such superficial modification provides the membranes super-hydrophilicity resulting in improved oil-water separation performance through time and oil rejection percentage while the membrane's fouling is negligible. Besides, the unique composition of these NPs brings a highly competitive catalytic activity (k_c factor) of 2.82 L $\cdot$ g^{-1} $\cdot$ s^{-1}, implying that their multifunctional nature could expand the cleansing capabilities of nanofibrous membranes by separating water from oily polluted sources and separately catalyze the degradation of water dissolved organic pollutants. Thus, providing a groundwork for future developments in the truly cleansing of oily polluted water.

Keywords: Oil-water separation, organic pollutants, laser ablation method, TiO, Ag nanoparticles PVDF membrane

1. Introduction

Every year thousands of oil tons are leaked and spilled into the oceans worldwide during the extraction and transportation of oil, making it the principal source of water pollution [1]. The toxic compounds in the oil represent serious health problems for humans and other living species [2]. As the oil sector represents an essential percentage of the global economy, the effective recovery of clean water from the oily polluted sources is a top priority for the scientific community. To date, the most common strategies used to treat oily polluted water are flotation, adsorption, gravity separation, coagulation, electrocoagulation, flocculation, membrane filtration, and very recently, oil capturing by the structural modification of surfaces and selective absorption and retention of water by the employment of super-amphiphilic materials like attapulgite (APT) [3-6]. Among the different alternatives, membrane filtration is the most popular because, in comparison with other systems, its usage is more accessible, cost-effective, and its employment leads to a minimal carbon footprint. However, the membranes need to fulfill essential characteristics to be useful in real situations like mechanical robustness, high flexibility, and chemical stability against harsh chemicals like halogens, oxidants, inorganic acids, aromatic, aliphatic, or chlorinated solvents, which are often involved in the water treatment [7].

Nanofiber-based membranes composed of highly resistant polymers like Polyvinylidene fluoride (PVDF), and Polyacrylonitrile (PAN), among others, substantially fulfill such requirements providing good oil-water separation performance driven by high porosity and low liquid flow resistance. However, they also get easily fouled because their structure allows the attachment and proliferation of bio-matter and macromolecules' allocation, among other foulants [8]. One of the primary ways to tackle such an issue is through the membrane's surface decoration with various kinds of NPs, among which those based on Ag and Ti stand above the rest. On the one hand, Ag NPs promote the membrane's surface charge change, super-hydrophilicity, and antibacterial behavior [9]. Ti-based NPs, on the other hand, provide super-lyophobicity, antifouling, antibacterial, and under ultraviolet illumination self-cleaning properties [10-12]. Thus, the membranes' decoration with these two NPs can significantly improve their oil-water separation performance. In the current work, we take a step forward, exploring the implications of tightly mixing these two NPs before the membranes' decoration. As it is well known, Ti-based NPs can act as supports for noble metals, providing them metal-support interactions (MSI) that are usually exploited in heterogeneous catalytic reactions like the degradation of organic pollutants [13,14]. When treating oily-polluted water, such an opportunity can provide the membranes a multifunctional surface that separately enhances their oil-water separation performance and contributes to organic pollutants' catalytic degradation. This overall can result in a critical benefit for the truly cleansing of polluted water, especially considering that most of the organic pollutants that contaminate all water sources easily dissolve in fats and oils [15].

To date, the methodologies that enable the tight combination of these two nanomaterials still fail in outshining their ecological benefit due to the employment of extreme conditions (high temperature and pressure) or toxic chemicals [16]. We are overcoming this barrier by employing reactive laser ablation in liquids (RLAL), a nanomaterials synthesis strategy not yet explored in the field that can bring many benefits. Its safety of operation and pollution suppressing nature make it suitable for such an environmentally conscious application [17]. Moreover, its most significant advantages over the classical synthesis approaches lie in the possibility of achieving tight junctions between almost any element, regardless of their miscibility, and due to the lack of capping or reducing agent usage, promise to get nanomaterials of the highest purity [18].

In short, when an ultra-short pulsed laser source (pulses in fs, i.e., 10^{-15} s) is used in RLAL, a solid target immersed in a liquid containing NPs-precursors (e.g., metal salts) absorbs the laser radiation, and due to a multiphoton-ionization mechanism, a plasma plume forms over the irradiated solid. The electrons in the plasma can induce the direct reduction of the NPs-precursors and create radicals that can also act as reducing agents. During and after the plasma lifetime, the species detached from the solid target and the reduced ones from the NPs-precursors combine, forming tight junctions. After the plasma extinguishes, a cavitation bubble forms containing all the plasma-constituent species; the bubble acts as a reactor where all these species keep experiencing coalescence, evolving into NPs that are released to the liquid medium when the bubble finally collapses [19].

Since the produced NPs are per se ligand-free [20], they can be anchored over nanofibrous membranes, finally permitting that when recovering water from oily polluted sources, the membrane's separation properties improve, and separately, the NPs-prompted degradation of organic pollutants dissolved in the oil and water takes place, resulting in the bettering of recovered water's quality. Overall, the current work presents the ad hoc design of a non-polluting solution for the possible deep cleansing of oily-polluted water, a global problem that is gradually leading to one of the worst crises in humankind history; the run-out of clean water.

2. Materials and methods

2.1. Membrane preparation

The membranes were prepared according to a previous study [21]. In brief, a needleless electrospinning system (Nanospider NS 8S1600U, Elmarco) was employed to make nanofibers of PVDF (13 wt %, Solef 1015), which was dissolved in N,N-dimethylformamide (DMF, Penta s.r.o.). The electrospun nanofibers were collected on a silicon paper and laminated by a heat-press at 130 °C (Pracovni Stroje, Teplice, Czech Republic) [22] to a supporting fabric with an adhesive web.
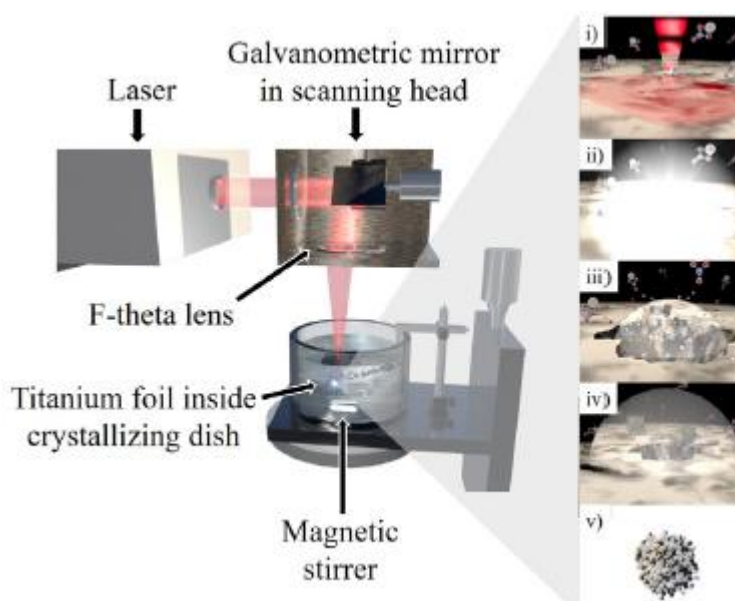

Fig. 1. Scheme depicting the elements of the experimental setup. Inset five images representing the follow-up of nanocomposite formation in RLAL. (i) absorption of laser radiation by the Ti solid target, (ii) creation of plasma plume above the irradiated area and reduction of NPs-precursors dispersed in the solvent, (iii) creation of the cavitation bubble, (iv) expansion of cavitation bubble, coalescence and formation of NPs, (v) final NPs released to the liquid medium.

The selected supporting fabric was a 100 g/m^2 spunbond PET nonwoven fabric with extremely high tensile strength and difficult to tear apart [23]. According to our previous studies, such robust support can transmit its mechanical stability to the PVDF nanofibrous membranes [22], thus, providing the possibility to get mechanically robust membranes. The surface of the membranes was further modified by their immersion for 1 h in a 1.8 M solution of potassium hydroxide (KOH, Fluka) in isopropanol (IPA, Fluka) at room temperature. The immersion in the KOH solution allowed the dehydrofluorination of the PVDF membrane and with this, its decoration with OH groups that enable the NPs attachment [21].

The Ag/TiO NPs were synthesized through the experimental set up displayed in **Fig. 1**. In brief, a Ti foil with a thickness of 0.025 mm (99.98% trace metals basis, Sigma-Aldrich) was selected as the solid target due to its ablation energy threshold is very low for fs pulses (0.5 µJ per pulse [24]), and the liquid medium was composed of a solution of silver nitrate (AgNO$_3$, Sigma-Aldrich) in deionized water (18.2 MΩ-cm). Since RLAL can assist the reduction of metal salts but it is still not completely understood how their concentration influences the atomic ratio of the final products, we employed a set of 6 different solution concentrations, where the resulting materials were labeled according to the used concentration: 0 mM (S1), 0.001 mM (S2), 0.01 mM (S3), 0.1 mM (S4), 1 mM (S5), and 10 mM (S6).

For performing RLAL, a laser beam was focused over the Ti foil placed in a holder immersed in 40 mL of the appropriate liquid solution while magnetically stirred at 100 rpm in a glass container. The laser beam came from a High-energy industrial fs laser Onefive Origamy XP-S (pulse duration 400 fs, central wavelength 1030 nm, and repetition rate 1 MHz). It was moved in a raster-like pattern at a velocity of 2 m/s by a scanning head (intelliSCAN 14, SCANLAB) and focused over the Ti foil surface by an f-theta lens with a focal length of 160 mm. The average power used was 150 mW, and the energy per pulse, 1.5 µJ, slightly overpassed the Ti ablation threshold to ensure that the AgNO$_3$ reduction would be a consequence of its interaction with the plasma plume and not due to other non-linear optical effects related to the use of high energies. After the irradiation of the whole Ti foil's surface (the process took 15 min), the solid target was removed from the glass container, and the membrane was placed inside in a vertical position. The recently produced nanocolloid kept being magnetically stirred for 2 h to ensure the maximum number of NPs anchor over the membrane. Afterward, the membrane was placed in a new glass container filled with deionized water, which was placed in an ultrasonic bath (SONOREX DIGITEC DT 510 H, 35 kHz, 9.7 L), and underwent ultrasonication for 10 min to get rid of the non-properly attached NPs. The labels used for the membranes decorated with the different NPs follow the syntax: M+S1, M+S2, M+S3, M+S4, M+S5, and M+S6.

2.2. NPs and membrane characterization

The NPs morphology was determined by transmission electron microscopy (TEM) using a microscope (JEM-2100Plus, JEOL) operated at an acceleration voltage of 200 kV. Their elemental composition was evaluated through energy-dispersive X-ray spectroscopy (EDX) using an analytical detector (X-Max 80, Oxford Instruments) attached to the TEM instrument. Likewise, an annular dark-field (HAADF) detector was employed to take dark-field images in Scanning TEM (STEM) mode and perform EDX fast mapping (FS mapping) and EDX line scans. Moreover, this information was ratified by single-particle inductively coupled plasma-mass spectrometry (spICP-MS) using a spectrometer (NexION 3000D, Perkin Elmer), which has a detection limit of 0.5 ng/L. The crystalline phases of the NPs were determined by X-ray powder diffraction (XRD) using a diffractometer (Miniflex 600, Rigaku) equipped with Co Kα radiation (λ = 0.1788 nm). The patterns were taken in a 2θ range 30-90° at a speed of 1° min^{-1}. The sample's absorbance was measured by visible spectroscopy using the same spectroscope employed in the degradation tests, but in this case, the absorbance was acquired in a range of 320-1000 nm in 1 nm

steps, and the samples' zeta potential values were acquired by a Zetasizer (Nano ZS90, Malvern Instruments Ltd).

The membranes' morphology was inspected by scanning electron microscopy (SEM) using a microscope (Vega3 SB, Tescan) operated at an acceleration voltage of 30 kV. The same micrographs were employed to roughly calculate the amount of NPs loading in the membranes. The membranes' pore size was determined through the bubble point method using a pore size analyzer (Porometer 3G, Anton Paar GmbH). The sample's wettability was determined by contact angle in air and underwater using a Drop Shape Analyser (DSA30E, Kruss GmbH). In the air, the droplets consisted of deionized water, and the measurements were taken at six different points of the sample's dry surface at room temperature. Underwater, the droplets consisted of kitchen oil and n-hexane; the measurement protocol was similar to the one in the air, except because the membranes were fixed to the bottom of a glass cuvette filled with deionized water by a double face tape, and the oil droplets were delivered through the tip of a 200 μL pipette after got in direct contact with the membrane. Finally, a complementary study was performed to assess the chemical stability of the PVDF nanofibrous membranes under harsh chemical conditions. For this, pristine PVDF membranes were immersed in an aqueous solution of 50% (w/v) NaOH [25], pure H_2O_2, and pure HCl for 3 weeks at room temperature. This test was not performed on the samples decorated by NPs because these chemicals at that concentration can digest the NPs [26]. After 3 weeks, the membranes were taken out, washed several times with distilled water, and dried at room conditions. Further, SEM images of the samples were taken to detect damages on the membrane surface.

2.3. Separation tests

Each sample's oil-water separation performance was evaluated by a custom-made dead-end filtration unit powered by gravity. The selected oil-water system was emulsion-type, where two of the most utilized oil-types in the field [27,28] served as the basis of the emulsion; sunflower kitchen oil from the market (100%, Goldplus), which physicochemical properties are not well controlled, but its use is widely extended, and n-hexane (pureness 99.0%, Penta s.r.o.), an oil with well known physicochemical properties.
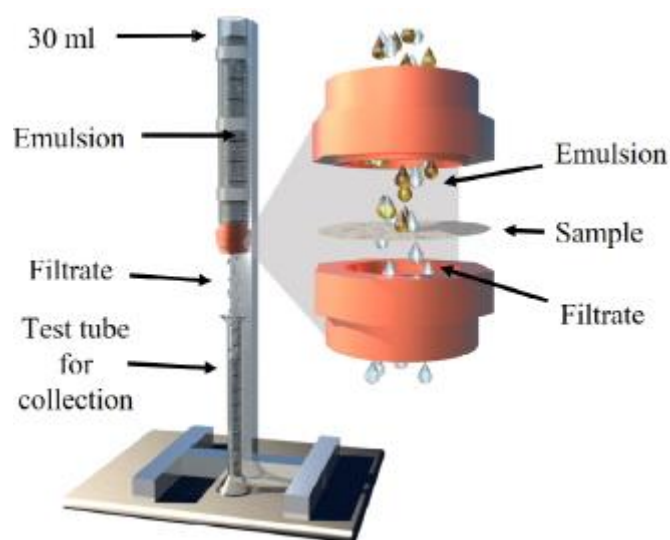

Fig. 2. Schematic representation of custom-made dead-end filtration unit powered by gravity. Inset it is displayed the position of the sample where the oil passage is avoided, and only the water is filtrated.

The preparation of each emulsion was done by mixing 400 mL of deionized water with 0.4 mL of the nonionic surfactant Triton X100 (laboratory-grade, Sigma-Aldrich) and 1 mL of the corresponding oil. The mixtures were stirred overnight at 600 rpm until a uniform emulsion was obtained. An optical microscope was employed to measure the emulsion uniformity and drop sizes (Axio Imager M2, Carl Zeiss), where the average oil droplets' diameter was (6.6 ± 3.1) pm for kitchen oil, and (2.0 ± 0.7) pm for n-hexane (Fig. S.1 in the Supporting Material).

The emulsion was used to feed the filtration unit from the open-top, and the level of feed was kept 30 cm above the membrane (diameter of 20 mm) as shown in **Fig. 2**. The emulsion filtration test was repeated 10 times (10 cycles) without changing the membrane to evaluate the sample's fouling resistance. Note that all the samples filtered 30 mL of deionized water before the emulsion test and between cycles. After separation, the permeate was analyzed by non-purgeable organic carbon (NPOC) measurements through a total carbon analyzer (MULTI N/C 2100S, Jena) to determine the residual amount of oil permeating through the membranes.

The membrane's permeate flux (F) and the permeability (k) were calculated according to the following set of formulas:

$$F = \frac{V}{A \cdot t} \tag{1}$$

$$k = \frac{F}{p} \tag{2}$$

where A represents the membrane area (m^2), V the permeate volume (in L units), p the trans-membrane pressure (0.03 bar in our case), and t the time of filtration (in h units). The sample's fouling was determined by the difference between the permeability values' at the first (k_i) and last filtration cycle (k_f) [29]:

$$Decline \quad in \quad permeability\,(\%) = \left(\frac{k_i - k_f}{k_i}\right) \times 100\% \tag{3}$$

The calculation of rejection ratio (R(%)) was done through the formula:

$$R\,(\%) = \left(1 - \frac{C_f}{C_i}\right) \times 100\% \tag{4}$$

where C_i is the carbon content in the original feed and C_f the one in the final permeate liquid after completing the separation cycles. Note that the C_f was taken after the tenth cycle to assess the robustness of the sample's filtration.

2.4. Catalytic tests

The NPs' catalytic activity was evaluated by reducing 4-nitrophenol (4-NP) to 4-aminophenol (4-AP), a model reaction to examine the power of metal-based catalysts. For this, the minimal required catalyst concentration was first assessed by a screening routine, where 0.12 mM of 4-NP (> 99% ReagentPlus, Sigma-Aldrich), 12 mM of sodium borohy-dride ($NaBH_4$, > 98%, Sigma-Aldrich), and various concentration of the nanocomposite (100.0, 50.0, 25.0, 12.5, and 6.3 mg/L) were mixed in deionized water at a volume of 1 mL and transferred to quartz cuvettes. The resultant liquid was analyzed by observing the intensity differences recorded at 400 nm by a spectrometer (DR 3900, Hach Lange). The continuous absorption decrement at this wavelength denotes the 4-NP reduction [30].

After identifying the sample displaying the best catalytic performance at the lowest concentration, three different concentrations of this catalyst (25.0, 12.5, and 6.3 mg/L) were used again to carry the 4-NP reduction. However, this time, the reaction mixtures with the same chemical ratios in a volume of 20 mL were magnetically stirred at 180 rpm and room temperature for the entire experiment. Aliquots were taken from the mixture at different intervals and filtered using syringe filters with a pore size of 0.22 μm (CHS Filterpure PTFE). The filtered aliquots were analyzed by high-performance liquid chromatography (HPLC) using a chromatograph (UltiMate 3000, Thermo Fisher Scientific) to observe in real-time the transformation from 4-NP into 4-AP. Both organic compounds were separated in the instrument through a Reprosher C18 column (150 mm length x 4.6 mm i.d., 3 μm particle size) at 40 °C. The mobile phase was composed of a 1:1 solution of deionized water and methanol (> 99.9% HPLC grade, Fisher Scientific), while the injection volume was 30 μl, and the flow rate 1 mL/min. The ultraviolet-visible (UV-Vis) detector (VWD-3100, Thermo Fisher Scientific) attached to the chromatograph was set to 230 nm to observe the simultaneous degradation of 4-NP and transformation into 4-AP [31]. The 4-NP degradation efficiency, conversion, and selectivity were calculated for the three employed catalyst concentrations through the following set of formulas:

$$Degradation\ efficiency\,(\%) = \left(\frac{c_i - c_t}{c_i}\right) \times 100\% \qquad (5)$$

$$Conversion\,(\%) = \left(\frac{amount\ of\ generated\ 4-AP}{amount\ of\ 4-NP\ used\ in\ the\ reaction}\right) \times 100\% \qquad (6)$$

$$Selectivity\,(\%) = \left(\frac{conversion}{degradation\ efficiency}\right) \times 100\% \qquad (7)$$

In formula (**5**), c_i represents the initial 4-NP concentration and c_t the concentration at a *t* time. In formula (**5**), ct represents the initial 4-NP concentration and ct the concentration at a *t* time. Finally, we implemented the so-called ''activity parameter'' k_c, which corresponds to the change of kinetic rate constants as a function of the catalyst dose to identify the total catalytic efficiency in our catalysts.

3. Results and discussion

3.1. Morphology and structure

Fig. 3 that displays representative images of the NPs indicates that, in general, the synthesis methodology leads to the production of principally small NPs surrounded by a low amount of larger

NPs, whether the liquid contains silver nitrate or not. hen using a laser with comparable pulses to the typical electron-phonon coupling time in metals (∼ ps), this type of morphology is found in NPs coming from the laser ablation in liquids. hen no metal salt is dispersed in the liquid environment, as the sample labeled S1, big particles' generation is due to hydrodynamic instabilities at the plasma plume-liquid interface and the small particles due to a subsequently expanding metal-liquid mixing region [32]. In the metal salts' presence, this kind of size distribution can be enriched by monometallic or bimetallic NPs. As recently explained by Tibbetts group [19] , when the laser intensity exceeds the liquid's optical breakdown (10^{13} /cm^2 for water), the liquid's molecules split, leading to many species like solvated electrons and hydrogen radicals that can reduce the metal salt for extended periods (∼10 ns - μs) resulting in the formation of large monometallic NPs.
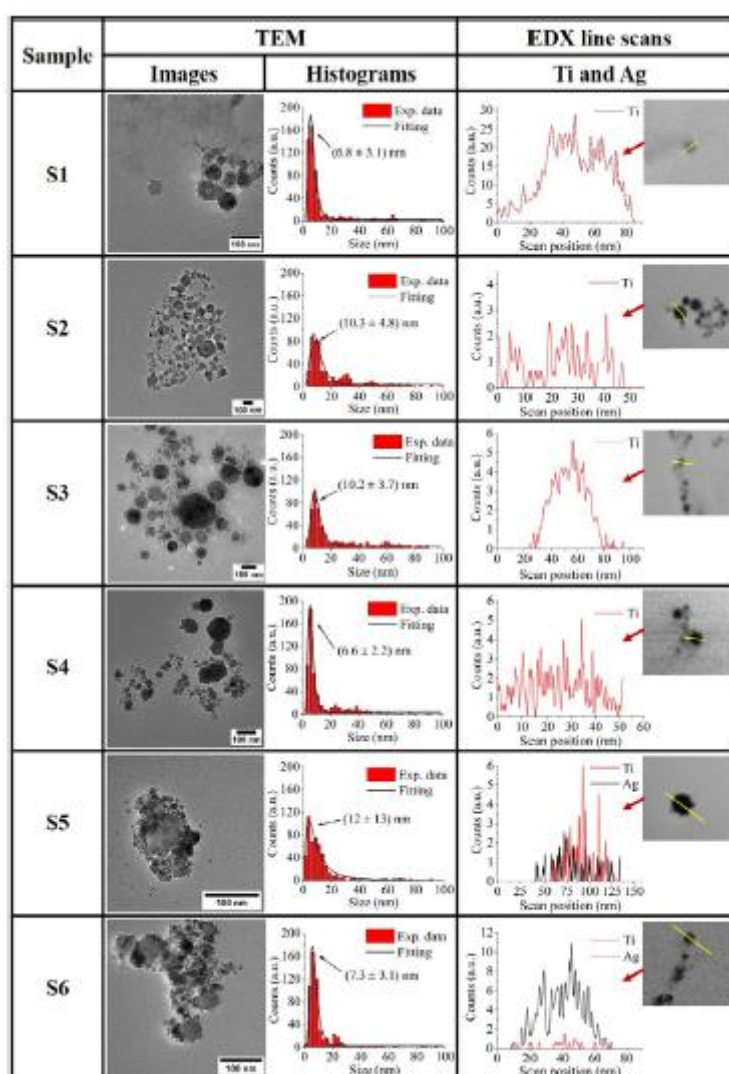

Fig. 3. List of representative TEM images, their size histograms considering the manual counting of at least 500 particles, and the EDX scan lines displaying only Ti and Ag elements to assess their distribution in the NPs. Inset the EDX scan line graphs it is displayed the particles where the corresponding scans were performed.

Small bimetallic particles in the counterpart arise from the interaction between the recently created NPs and the liquid medium after their ablation-driven ejection. During the interaction with the liquid, the NPs can rapidly oxidize, providing nucleation sites for the metal salts.

Since the laser intensity employed during the current work, $\sim 1.3 \cdot 10^{10}$ /cm^2, did not reach the value required to split the water molecules, it is more probable to find the Ti and Ag elements in the smaller particles and only Ti in the larger once. Besides, according to the spICP-MS results extracted from individual particles (Tab. S.1 in the Supplementary Material), silver nitrate concentrations below the mM unity result in NPs containing less than 10 wt% of Ag, explaining in this way their lack of visualization in the EDX-Maps and EDX scan lines (Fig. S.2 in the Supplementary Material). Moreover, the maximized salt's abundance in the sample 10 mM results in overexpression of Ag in the composites by more than 80 wt%. This fact indicates that the initial salt concentration has a critical impact on the final NPs chemical composition when using laser intensities lower than the one required to reach the liquid's optical breakdown, being 1 mM the threshold for fine chemical composition control.

As observed in **Fig. 4**, the NPs chemical composition also has a critical influence on the membrane's decoration, where those having a more extensive content of Ag seem to get more firmly attached to the membrane's surface, leading to a final loading of $2.32 \cdot 10^{11}$ particles/cm^2 or 0.36 µg/cm^2 for S6, $1.86 \cdot 10^{11}$ particles/cm^2 or 0.38 µg/cm^2 for S5, $1.31 \cdot 10^{11}$ particles/cm^2 or 0.13 µg/cm^2 for S4, $7.12 \cdot 10^{10}$ particles/cm^2 or 0.25 µg/cm^2 for S3, $9.20 \cdot 10^{9}$ particles/cm^2 or 0.03 µg/cm^2 for S2, and $4.34 \cdot 10^{10}$ particles/cm^2 or 0.04 µg/cm^2 for S1.
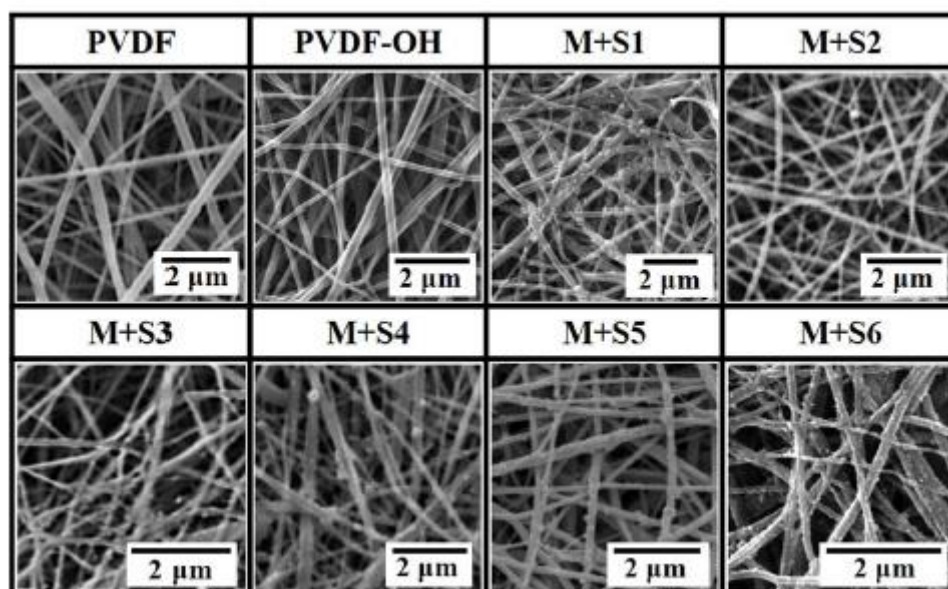

Fig. 4. List of representative SEM images of the membranes decorated with the NPs.

Note that the approximate weight loading values are calculated considering that the atomic radius and weight of Ag and Ti are 144 pm, 107.87 g/mol, and 176 pm, 47.87 g/mol, respectively. The circular membranes' diameter is 2 cm, and the NPs size and element ratio correspond to those obtained by spICP-MS and TEM analysis. Thus, given the structural and morphological variations among the samples, the weight loading does not increase continuously as the number of attached particles does.

As revealed by the XRD measurements (Fig. S.3 in the Supplementary Material), the detected crystalline phases in the samples are the face-centered cubic crystalline phase $TiO_{1.04}$ (JCPDS database: PDF-00-043-1296), the rhombohedral crystal phase Ti_2O_3 (JCPDS database: PDF-10-63), and the face-centered cubic phase of Ag (JCPDS database: 00-004-0783). Since hydroxyl groups are the functionalities employed to immobilize the particles, it is expected that the samples with a more extensive content of Ag attach more strongly to the membranes. This is due to stronger covalent

binding between Ag and the OH- groups [33], in contrast to the weaker hydrogen bonding between the membrane's OH- groups and those formed around the Ti oxides when exposed to water [34].

Although the particles' load is more prominent when the Ag content increases, the membranes' pore size, which directly impacts the oil droplets' free passage due to the ''size-sieving'' effect, does not seem to be heavily affected. As observed in **Table 1**, the modified membranes have a slightly smaller average pore size in comparison to the pristine PVDF one. This pore size minimal reduction can be attributed, as previously reported [21], to the membrane's microstructural shrinkage resulting from the dehydrofluorination process. Even though the pore size reduction is minimal, such modification can enhance the oil rejection mechanism based on the size-sieving effect to avoid the passage of the kitchen oil and n-hexane droplets, which sizes exceed the samples' pore sizes by one order of magnitude. Note that if necessary, the pore size can also be increased by exposing the membranes to increments in temperature [21], thus, allowing a modification in the membranes' droplet-size selectivity.

Besides, the samples' wettability, which constitutes the second mechanism involved in the free-passage of water and repellence of oil droplets, shows a very different behavior between samples. As displayed in **Table 1**, contrary to previous studies, the massive inkrement of Ag in the NPs does not seem to have a beneficial impact on the dried membrane's hydrophilicity.

Table 1 Average pore size and contact angle measurements in air and underwater for kitchen oil and n-hexan

Sample	Pore size (µm)	Contact angle (°)		
		In air	Underwater	
			kitchen oil	n-hexane
PVDF	0.40 ± 0.01	125.9	37.7	0.0
PVDF-OH	0.37 ± 0.01	92.5	43.4	66.3
M+S1	0.37 ± 0.01	90.4	30.5	54.7
M+S2	0.34 ± 0.01	95.4	47.5	50.0
M+S3	0.32 ± 0.01	99.9	40.5	0.0
M+S4	0.34 ± 0.01	0	No adhesion	No adhesion
M+S5	0.32 ± 0.01	91.7	No adhesion	No adhesion
M+S6	0.38 ± 0.01	110.1	No adhesion	No adhesion

As described elsewhere, Ag NPs can be oxidized by dissolved oxygen in water according to the following reaction [35], followed by Ag$^+$ release:

$$2Ag_{(s)} + \frac{1}{2}O_{2(aq)} + 2H^+_{(aq)} \rightleftharpoons 2Ag^+_{(aq)} + H_2O \qquad (8)$$
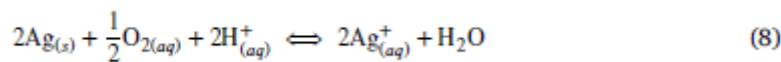
where Ag$_{(s)}$ refers to the Ag NPs, and the subscript *(aq)* dissolved in water. After their release, the hydrated ions eventually adsorb over the membrane's surface, enhancing its hydrophilicity [36]. Since the key factor that renders the membranes' hydrophilic behavior is the adhesion of the polar water molecules over a positively charged surface, the larger amount of Ag should also mean a larger amount of adsorbed Ag$^+$ over the membrane's surface and enhanced hydrophilicity. This effect is only visible in the M+S4 sample, which, aside from providing super-hydrophilicity (0° contact angle), also turn the membrane's surface oleophobic regardless of the type of oil. Conversely, in contrast with our previous study [21], the larger NPs load found in M+S5 seems to be disadvantageous for breaking the water droplet's surface tension by providing many low contact area sites [37]. However, as proven by the underwater oil contact angle data, it is advantageous for providing oleophobicity. A larger NPs load,

like the one found in M+S6 seems to provide a larger number of low contact area sites, finally turning the membrane into both hydrophobic and oleophobic. Therefore, as observed in **Table 1**, the limit of NPs load number to avoid turning dry membranes into hydrophobic, which may be potentially harmful to the membranes' oil-water separation performance is $1.31 \cdot 10^{11}$ particles/cm^2.

Finally, the side membranes' chemical stability study demonstrates that the exposure of the pristine PVDF membranes to harsh chemical conditions does not seem to result in their degradation (see Fig. S.4 in the Supplementary Material). Thus, allowing us to ratify their parallel suitability for water recovery from oily polluted sources and usefulness as support in processes such as the catalytic degradation of organic pollutants dissolved in water and oil, which take place in chemically demanding conditions.

3.2. Oil–water separation performance

The emulsion membranes' permeability and oil rejection presented in **Fig. 5** shows that the permeability of all the samples starts in high values, following the tendency M+S5 > M+S2, M+S3 > M+S4, M+S1, PVDF-OH > M+S6 > PVDF for kitchen oil, and M+S1 > M+S5 > PVDF-OH > PVDF, M+S2, M+S3, M+S6 > M+S4 for n-hexane. However, it later decreased through the time exponentially during the first 8 cycles and then stabilized at permeability values with the tendency M+S5 > PVDF-OH, M+S1, M+S2, M+S3 > PVDF, M+S4, M+S6 for kitchen oil, and PVDF-OH > PVDF, M+S1, M+S2, M+S3, M+S5, M+S6 > M+S4 for n-hexane. The permeability decrement can be attributed to the concentration of oil droplets near the membrane difficulting the water's free pass. Since the gravity force powers the separation setup, the oils can form a layer of separated small oil droplets. Thus, when the oil layer reaches its saturation thickness, the permeability reaches its stability. Given the current results, a NPs load of $1.86 \cdot 10^{11}$ particles/cm2 or 0.38 µg/cm^2 composed of 31.22 wt% of Ag and 68.78 wt% of Ti seem to be ideal for reaching the maximum membrane's permeability, additionally demonstrating that a pressure value of 0.03 bar can effectively overcome the water's surface tension, and with this, get access to the wettability properties provided by both elements. Membranes' surface charge increment by Ag$^+$ adsorption and hydroxyl groups formed over the Ti oxides. As discussed above, in the case of Ag+, they can increment the positive charge in the membrane, and in the case of the Ti oxides' hydroxyl groups, they can increment the membranes' surface positive or negative charge depending on the medium's pH (positive for small pH and negative for a high one) [**38**]. Since the emulsion elements do not change the deionized water's pH (pH = 7), the S5 NPs should overall provide a positive surface charge to the membrane boosting the attraction of the polar water molecule and subsequent permeability.

The decline in permeability (**Fig. 5**) and the rejection rate data (**Table 2**) enables understanding that even when M+S5 displays the best permeability performance regardless of the oil, it is not the best option for long-term use. According to these data, S4 NPs with a load of $1.31 \cdot 10^{11}$ particles/cm^2 or 0.13 µg/cm^2 seem to provide the overall best antifouling performance and oil rejection, thus, leading to improved long-term stability. This fact demonstrates that even when an element combination of 31.22 wt% of Ag and 68.78 wt% of Ti in the decorating NPs provides the most considerable permeability to the PVDF membranes, rendered by an optimal combination of surface wettability and small pore size, this can be spoiled by a small increment in the NPs load. As observed in the contact angle tests, the slight difference of $5.50 \cdot 10^{10}$ particles/cm^2 between M+S4 and M+S5 can lead to a rougher surface, which can permit the allocation of foulants over the membrane's surface. Even when the membranes' wettability and pore size oppose the oil leaching through them, this oil allocation can also result in the opposite [**39**]. As displayed in Fig. S1 (in the Supplementary Material), the emulsified oils present a

wide droplet size distribution. Thus, during the oil allocation, a large number of oil droplets of similar size to the membranes' pores could concentrate over the membranes' surface, and with the help of the trans-membrane pressure, overcome the rejection barrier imposed by the size-sieving and water adsorption effects. Such a fact is exalted by the rejection rate difference between oils, where n-hexane with the droplets' smallest size generally leads to the lowest rejection rate values, except for M+S4, whose ability to avoid oil allocation enhances its rejection rate. Besides, the further loading increment of $4.60 \cdot 10^{10}$ particles/cm^2 found in M+S6 compared to M+S5 can provide sufficient roughness to avoid the oil droplets allocation but also, due to the hydrophobicity, impose resistance to the free pass of water, reducing both the membranes' permeability and fouling.
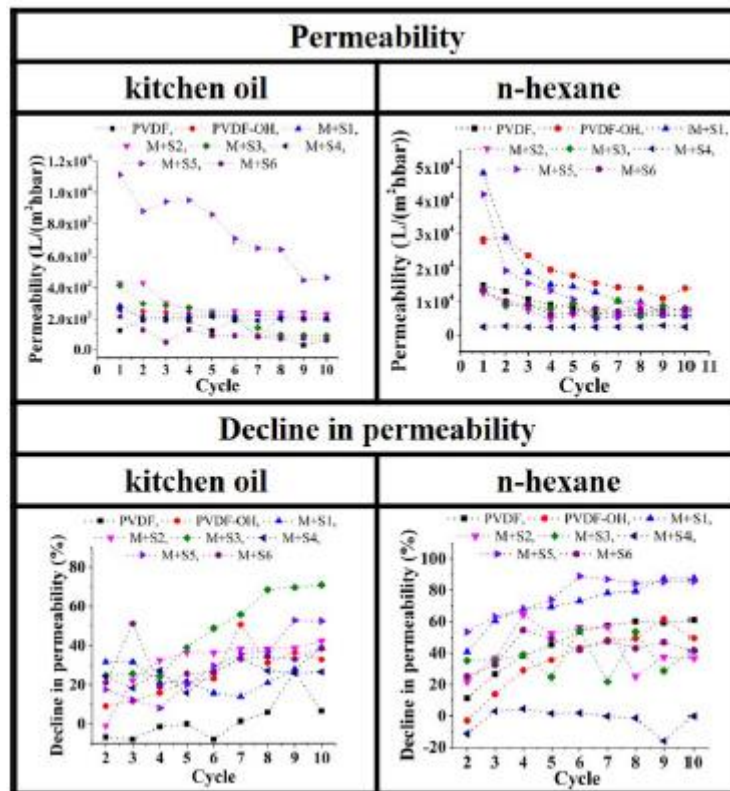

Fig. 5. Graphs summarizing the permeability and decline in permeability results from each sample. On the left side, it is possible to observe the data after separation from kitchen oil, and on the right side, the data after separation from n-hexane.

Table 2 Membranes' rejection rate R(%) of kitchen oil and n-hexane.

Sample	Rejection rate (%)	
	kitchen oil	n-hexane
PVDF	88.7	80.7
PVDF-OH	92.7	81.0
M+S1	96.4	80.0
M+S2	97.0	87.3
M+S3	96.1	91.4
M+S4	97.9	92.3
M+S5	93.0	90.7
M+S6	94.3	90.4

Therefore, the current data provide the valuable lesson that the combination of the membranes' pore size and surface chemistry of the NPs has a positive effect on the long-term oil-water efficiency when the loading does not exceed the NPs number limit of $1.31 \cdot 10^{11}$ particles/cm^2.

3.3. NPs' catalytic performance

The performed screening routine (Fig. S.5 in the Supplementary Material) enables understanding that the sample labeled S4 displays the best kinetic reaction constant for the lowest concentration when used as the catalyst in the transformation from 4-NP to 4-AP by catalytic hydrogenation where NaBH4 acts as the hydrogen donor. As it is widely accepted, the core role of metal NPs when acting as catalysts in this reaction relies on the hydrogen adsorption from the sodium borohydride and 4-NP over their surface. The catalyst then enables a 6-electron powered reaction where the 4-NP reduces to a nitroso compound, that later reduces to its corresponding hydroxylamine, and finally to 4-AP [40] as represented in **Fig. 6**. Note that, since NaBH$_4$ was used in a large amount compared to 4-NP, it can be considered constant during the reaction.
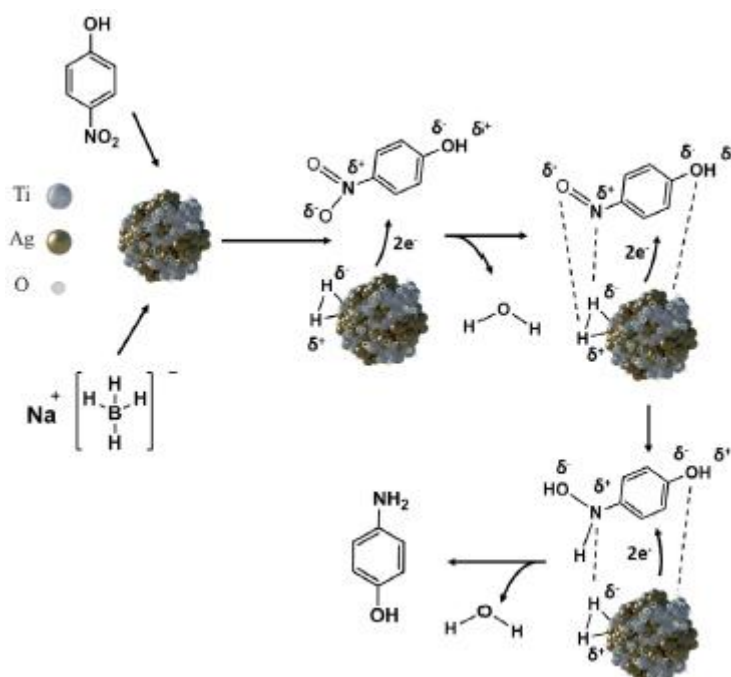

Fig. 6. Sketch representing the stepwise reduction of 4-NP to 4-AP when Ag/TiO NPs act as the catalyst agent, and NaBH4 as the hydrogen donor.

As recently recognized by Imran M. and co-workers [**14**], when a nonstoichiometric crystal with a large concentration of oxygen vacancies like TiO$_{1.04}$ acts as the support of noble metal NPs, the delocalized electrons in the TiO vacancies facilitate the dissociative adsorption of H$_2$ from NaBH$_4$ over Ag NPs, boosting in this way the material's catalytic power in the transformation from 4-NP to 4-AP. Since the larger amount of these MSI should lead to the best catalytic performance, it is understandable that S4 revealed itself as the best catalyst. On the one hand, EDX line scans display together with their absorbance spectra (Fig. S.6 in the Supplementary Material) that only the samples S4, S5, and S6 seem to have a core-shell type elemental distribution where Ag forms part of the NPs shell and the Ti species the core. Note that in case of S4, the minimal presence of Ag does not allow to observe the Ag signal by the EDX detector, but the surface plasmon resonance (SPR) activity, which requires the presence of

a noble metal in the surface to occur, evidences the elemental distribution in this sample. On the other hand, as exhibited by XRD and spICP-MS measurements, TiO presence is maximized for S4, thus, the number of MSI, and with this the overall catalytic activity.

Fig. 7 showing that in general, the S4 NPs can convert the 4-NP to 4-AP with 100% efficiency and selectivity, even at a minimum concentration of 6.3 mg/L, points out that this sample has a competent catalytic behavior for large or low concentrations. Thus, they can be suitable candidates to provide catalytic activity to the membranes understudy, which require minimal NPs loading. Finally, as the k_c parameter extracted from the slope of the fitting line in **Fig. 7**d) is 2.82 L g^{-1} s^{-1}, it is possible to say that the absolute catalytic activity of S4 is comparable to that of the latest Ag catalysts found in the literature [**41-43**]. Therefore, such nanomaterial employment in nanofibrous membranes' decoration can not only improve their oil-water separation performance by providing optimal wettability, loading, and antifouling properties, but due to the many catalytic active sites in Ag/TiO NPs it can potentially lead to the simultaneous catalytic removal of pollutants dissolved in oily polluted sources.

4. Conclusions

To summarize, we have employed the light-powered synthesis methodology known as RLAL to produce for the first time Ag/TiO NPs with controlled elemental composition while suppressing chemical waste production, which is often associated with the creation of such nanostructures.
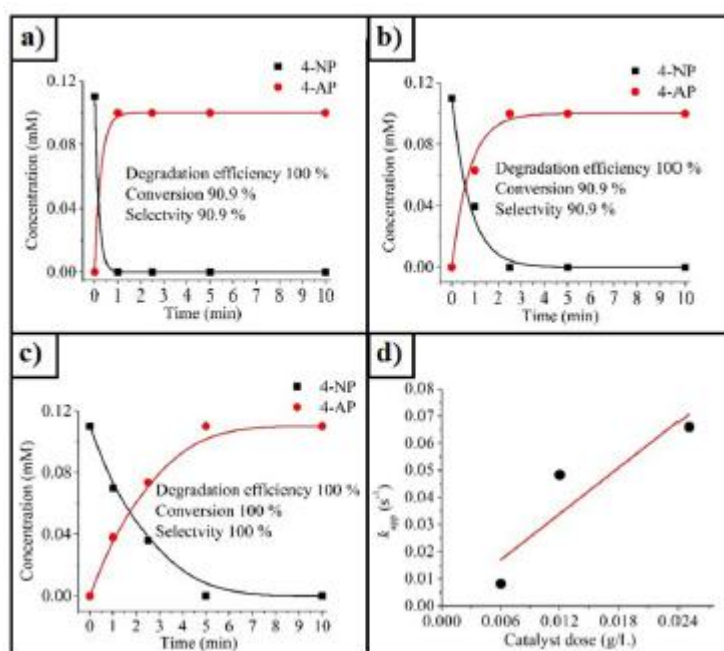

Fig. 7. Evolution of 4-NP transformation to 4-AP using S4 NPs as catalysts, (a) corresponds to the concentration of 25.0 mg/L, (b) to 12.5 mg/L, and (c) to 6.3 mg/L. Besides, (d) displays the change of kinetic rate constants as a function of the catalyst dose.

Since Ag and Ti-oxide species have properties in high demand for improving robust membranes exploited in the recovery of clean water from oily polluted sources, we took the decoration of the highly resistant against harsh conditions PVDF nanofibrous membranes by these two elements as the study subject. However, unlike the plain perspective where separate NPs of distinct nature are

employed for the decoration, we decided to take a step forward by exploring the implication of using NPs that tightly mix these two elements. Our results indicate that NPs with an average size of (6.6 ± 2.2) nm, an element composition of 93.79 wt% Ti, and 6.21 wt% Ag, where the Ag is located at the NPs exterior side, can bring the most improving qualities to the membranes. On the one hand, this elemental composition and morphology enable the optimal loading of $1.31 \cdot 10^{11}$ particles/cm^2 or 0.13 μg/cm^2, which brings an ideal wettability that, in combination with the membranes' pore size, results in avoiding the long-term pass of oil droplets through the membranes regardless of the oil's nature. However, it is essential to recognize that given the mechanisms involved in the oil-water separation, i.e., water adsorption and size-sieving effects, the oil rejection barrier formed by the NPs decorated membranes could be potentially surpassed by oil droplets with comparable or tinier sizes than the membranes' pores. On the other hand, these same NPs also display the most potent catalytic performance reaching a remarkable kc value of 2.82 L g^{-1} s^{-1}, presumably because their element composition and distribution vastly increase the number of MSI compared to the rest of the samples, translating into enhanced catalytic activity. Therefore, the antifouling properties provided to the membranes understudy and the possibility of employing them as supports for degrading, in parallel, organic pollutants commonly found in polluted water, open up the prospect of recovering clean water from oily polluted sources. Given these findings, the current study brings new insights to the efficient design of ad hoc nanomaterials for the improvement of membranes and establishes the ground for future developments in the truly cleansing of oily polluted water.

References

[1]   M. Ge, C. Cao, J. Huang, X. Zhang, Y. Tang, X. Zhou, K. Zhang, Z. Chen, Y. Lai, Rational design of materials interface at nanoscale towards intelligent oil-water separation, Nanoscale Horiz. 3 (3) (2018) 235-260, **http://dx.doi.org/10.1039/ C7NH00185A**.

[2]   C.P. Brussaard, L. Peperzak, S. Beggah, L.Y. Wick, B. Wuerz, J. Weber, J.S. Arey, B. Van Der Burg, A. Jonas, J. Huisman, et al., Immediate ecotoxicological effects of short-lived oil spills on marine biota, Nature Commun. 7 (1) (2016) 1-11, **http://dx.doi.org/10.1038/ncomms11206**.

[3]   Z. Chu, Y. Feng, S. Seeger, Oil/water separation with selective superanti-wetting/superwetting surface materials, Angew. Chem. Int. Ed. 54 (8) (2015) 2328-2338, **http://dx.doi.org/10.1002/anie.201405785**.

[4]   L. Mohammadi, A. Rahdar, E. Bazrafshan, H. Dahmardeh, M. Susan, A.B. Hasan, G.Z. Kyzas, Petroleum hydrocarbon removal from wastewaters: A review, Processes 8 (4) (2020) 447, **http://dx.doi.org/10.3390/pr8040447**.

[5]   H. Li, P. Mu, J. Li, Q. Wang, Inverse desert beetle-like ZIF-8/PAN composite nanofibrous membrane for highly efficient separation of oil-in-water emulsions, J. Mater. Chem. A 9 (7) (2021) 4167-4175, **http://dx.doi.org/10.1039/ D0TA08469G**.

[6]   M. Cui, P. Mu, Y. Shen, G. Zhu, L. Luo, J. Li, Three-dimensional attapulgite with sandwich-like architecture used for multifunctional water remediation, Separation Purif. Technol. 235 (2020) 116210, **http://dx.doi.org/10.1016/j. seppur.2019.116210**.

[7]   N.A. Hashim, Y. Liu, K. Li, Stability of PVDF hollow fibre membranes in sodium hydroxide aqueous solution, Chem. Eng. Sci. 66 (8) (2011) 1565-1575, **http://dx.doi.org/10.1016/j.ces.2010.12.019**.

[8]   M. Padaki, R.S. Murali, M.S. Abdullah, N. Misdan, A. Moslehyani, M. Kassim, N. Hilal, A. Ismail, Membrane technology enhancement in oil-water separation. A review, Desalination 357 (2015) 197-207, **http://dx.doi.org/10.1016/j.desal. 2014.11.023**.

[9]   M.S.S.A. Saraswathi, D. Rana, S. Alwarappan, S. Gowrishankar, P. Vijayaku-mar, A. Nagendran, Polydopamine layered poly (ether imide) ultrafiltration membranes tailored with silver nanoparticles designed for better permeability, selectivity and antifouling, J. Ind. Eng. Chem. 76 (2019) 141-149, **http://dx.doi. org/10.1016/j.jiec.2019.03.014**.

[10]   M. Wu, G. Shi, W. Liu, Y. Long, P. Mu, J. Li, A universal strategy for the preparation of dual superlyophobic surfaces in oil-water systems, ACS Appl. Mater. Interfaces 13 (12) (2021) 14759-14767, **http://dx.doi.org/10.1021/ acsami.1c02187**.

[11]   Z.-M. Zhang, Z.-Q. Gan, R.-Y. Bao, K. Ke, Z.-Y. Liu, M.-B. Yang, W. Yang, Green and robust superhydrophilic electrospun stereocomplex polylactide membranes: Multifunctional oil/water separation and self-cleaning, J. Membr. Sci. 593 (2020) 117420, **http://dx.doi.org/10.1016/j.memsci.2019.117420**.

[12]   M. Zimbone, M. Buccheri, G. Cacciato, R. Sanz, G. Rappazzo, S. Boninelli, R. Reitano, L. Romano, V. Privitera, M. Grimaldi, Photocatalytical and antibacterial activity of TiO2 nanoparticles obtained by laser ablation in water, Appl. Catal. B 165 (2015) 487-494, **http://dx.doi.org/10.1016/j.apcatb.2014.10.031**.

[13]   M. Comotti, W.-C. Li, B. Spliethoff, F. Schuth, Support effect in high activity gold catalysts for CO oxidation, J. Am. Chem. Soc. 128 (3) (2006) 917-924, **http://dx.doi.org/10.1021/ja0561441**.

[14]   M. Imran, A.B. Yousaf, X. Zhou, Y.-F. Jiang, C.-Z. Yuan, A. Zeb, N. Jiang, A.-W. Xu, Pd/TiO nanocatalyst with strong metal-support interaction for highly efficient durable heterogeneous hydrogenation, J. Phys. Chem. C 121 (2) (2017) 1162-1170, **http://dx.doi.org/10.1021/acs.jpcc.6b10274**.

[15]   A.M. Pintor, V.J. Vilar, C.M. Botelho, R.A. Boaventura, Oil and grease removal from wastewaters: sorption treatment as an alternative to state-of-the-art technologies. A critical review, Chem. Eng. J. 297 (2016) 229-255, **http://dx.doi. org/10.1016/j.cej.2016.03.121**.

[16]   H. Miyamura, S. Kobayashi, Tandem oxidative processes catalyzed by polymer-incarcerated multimetallic nanoclusters with molecular oxygen, Acc. Chem. Res. 47 (4) (2014) 1054-1066, **http://dx.doi.org/10.1021/ar400224f**.

[17]   V. Amendola, I.D. Amans, Y. Ishikawa, N. Koshizaki, S. Scire, G. Compagnini, S. Reichenberger, I.S. Barcikowski, Room-temperature laser synthesis in liquid of oxide, metal-oxide core-shells, and doped oxide nanoparticles, Chemistry (Weinheim An Der Bergstrasse, Germany) 26 (42) (2020) 9206, **http://dx.doi. org/10.1002/chem.202000686**.

[18]   A. Chemin, J. Lam, G. Laurens, F. Trichard, V. Motto-Ros, G. Ledoux, V. Jary, V. Laguta, M. Nikl, C. Dujardin, et al., Doping nanoparticles using pulsed laser ablation in a liquid containing the doping agent, Nanoscale Adv. 1 (10) (2019) 3963-3972, **http://dx.doi.org/10.1039/C9NA00223E**.

[19]   M.G. John, K.M. Tibbetts, One-step femtosecond laser ablation synthesis of sub-3 nm gold nanoparticles stabilized by silica, Appl. Surf. Sci. 475 (2019) 1048-1057, **http://dx.doi.org/10.1016/j.apsusc.2019.01.042**.

[20] D. Zhang, B. Gokce, S. Barcikowski, Laser synthesis and processing of colloids: fundamentals and applications, Chem. Rev. 117 (5) (2017) 3990-4103, **http://dx.doi.org/10.1021/acs.chemrev.6b00468**.

[21] R. Torres-Mendieta, F. Yalcinkaya, E. Boyraz, O. Havelka, S. Wacławek, J. Maryška, M. Černík, M. Bryjak, PVDF nanofibrous membranes modified via laser-synthesized Ag nanoparticles for a cleaner oily water separation, Appl. Surf. Sci. 526 (2020) 146575, **http://dx.doi.org/10.1016/j.apsusc.2020.146575**.

[22] R. Roche, F. Yalcinkaya, Incorporation of PVDF nanofibre multilayers into functional structure for filtration applications, Nanomaterials 8 (10) (2018) 771, **http://dx.doi.org/10.3390/nano8100771**.

[23] F. Yalcinkaya, B. Yalcinkaya, J. Hruza, P. Hrabak, Effect of nanofibrous membrane structures on the treatment of wastewater microfiltration, Sci. Adv. Mater. 9 (5) (2017) 747-757, **http://dx.doi.org/10.1166/sam.2017.3027**.

[24] B. Gakovic, G. Tsibidis, E. Skoulas, S.M. Petrovic, B. Vasic, E. Stratakis, Partial ablation of Ti/Al nano-layer thin film by single femtosecond laser pulse, J. Appl. Phys. 122 (22) (2017) 223106, **http://dx.doi.org/10.1063/1.5016548**.

[25] J. Speight, Industrial inorganic chemistry, Environ. Inorg. Chem. Eng. (2017) 111-169, **http://dx.doi.org/10.1016/B978-0-12-849891-0.00003-5**.

[26] A.-L. Fabricius, L. Duester, B. Meermann, T.A. Ternes, ICP-MS-Based characterization of inorganic nanoparticles—sample preparation and off-line fractionation strategies, Anal. Bioanal. Chem. 406 (2) (2014) 467-479, **http://dx.doi.org/10. 1007/s00216-013-7480-2**.

[27] M. Qu, Q. Liu, J. He, J. Li, L. Liu, C. Yang, X. Yang, L. Peng, K. Li, A multifunctional superwettable material with excellent pH-responsive for controllable in situ separation multiphase oil/water mixture and efficient separation organics system, Appl. Surf. Sci. 515 (2020) 145991, **http://dx.doi.org/10.1016/j.apsusc. 2020.145991**.

[28] K. Venkatesh, G. Arthanareeswaran, A. Chandra Bose, P. Suresh Kumar, J. Kweon, Diethylenetriaminepentaacetic acid-functionalized multi-walled carbon nanotubes/titanium oxide-PVDF nanofiber membrane for effective separation of oil/water emulsion, Separation Purif. Technol. 257 (2021) 117926, **http://dx.doi.org/10.1016/j.seppur.2020.117926**.

[29] S. Pourziad, M.R. Omidkhah, M. Abdollahi, Improved antifouling and selfcleaning ability of PVDF ultrafiltration membrane grafted with polymer brushes for oily water treatment, J. Ind. Eng. Chem. 83 (2020) 401-408, **http://dx.doi. org/10.1016/j.jiec.2019.12.0**.

[30] J. Yu, W. Niedenthal, B.M. Smarsly, M.M. Natile, Y. Huang, M. Carraro, Au nanoparticles supported on piranha etched halloysite nanotubes for highly efficient heterogeneous catalysis, Appl. Surf. Sci. 546 (2021) 149100, **http://dx.doi.org/10.1016/j.apsusc.2021.149100**.

[31] K. Krawczyk, S. Wacławek, D. Silvestri, V.V. Padil, M. Řezanka, M. Černík, M. Jaroniec, Surface modification of zero-valent iron nanoparticles with ^-cyclodextrin for 4-nitrophenol conversion, J. Colloid Interface Sci. (2020) 655-662, **http://dx.doi.org/10.1016/j.jcis.2020.10.135**.

[32] C.-Y. Shih, R. Streubel, J. Heberle, A. Letzel, M.V. Shugaev, C. Wu, M. Schmidt, B. Gokce, S. Barcikowski, L.V. Zhigilei, Two mechanisms of nanoparticle generation in picosecond laser

ablation in liquids: The origin of the bimodal size distribution, Nanoscale 10 (15) (2018) 6900-6910, **http://dx.doi.org/10.1039/ C7NR08614H**.

[33]   A.K. Thompson, C. Hackett, T.L. Grady, S. Enyinnia, Q.C. Moore, F.M. Nave, Development and characterization of membranes with PVA containing silver particles: A study of the addition and stability, Polymers 12 (9) (2020) 1937, **http://dx.doi.org/10.3390/polym12091937**.

[34]   T. Hanawa, Transition of surface modification of titanium for medical and dental use, in: Titanium in Medical and Dental Applications, Elsevier, 2018, pp. 95-113, **http://dx.doi.org/10.1016/B978-0-12-812456-7.00005-6**.

[35]   J. Liu, R.H. Hurt, Ion release kinetics and particle persistence in aqueous nanosilver colloids, Environ. Sci. Technol. 44 (6) (2010) 2169-2175, **http://dx.doi. org/10.1021/es9035557**.

[36]   J.-H. Li, X.-S. Shao, Q. Zhou, M.-Z. Li, Q.-Q. Zhang, The double effects of silver nanoparticles on the PVDF membrane: Surface hydrophilicity and antifouling performance, Appl. Surf. Sci. 265 (2013) 663-670, **http://dx.doi.org/10.1016/j. apsusc.2012.11.072**.

[37]   A. Valsesia, C. Desmet, I. Ojea-Jiménez, A. Oddo, R. Capomaccio, F. Rossi, P. Colpo, Direct quantification of nanoparticle surface hydrophobicity, Commun. Chem. 1 (1) (2018) 1-11, **http://dx.doi.org/10.1038/s42004-018-0054-7**.

[38]   T.W. Healy, D.W. Fuerstenau, The oxide-water interface—Interrelation of the zero point of charge and the heat of immersion, J. Colloid Sci. 20 (4) (1965) 376-386, **http://dx.doi.org/10.1016/0095-8522(65)90083-8**.

[39]   M. Li, L. Wu, C. Zhang, W. Chen, C. Liu, Hydrophilic and antifouling modification of PVDF membranes by one-step assembly of tannic acid and polyvinylpyrrolidone, Appl. Surf. Sci. 483 (2019) 967-978, **http://dx.doi.org/10.1016/j.apsusc. 2019.04.057**.

[40]   M. Ismail, M. Khan, S.B. Khan, K. Akhtar, M.A. Khan, A.M. Asiri, Catalytic reduction of picric acid, nitrophenols and organic azo dyes via green synthesized plant supported Ag nanoparticles, J. Molecular Liquids 268 (2018) 87-101, **http://dx.doi.org/10.1016/j.molliq.2018.07.030**.

[41]   Z. Zheng, Q. Huang, H. Guan, S. Liu, In situ synthesis of silver nanoparticles dispersed or wrapped by a Cordyceps sinensis exopolysaccharide in water and their catalytic activity, RSC Adv. 5 (85) (2015) 69790-69799, **http://dx.doi.org/ 10.1039/C5RA09452F**.

[42]   T.K. Das, S. Ganguly, P. Bhawal, S. Mondal, N.C. Das, A facile green synthesis of silver nanoparticle-decorated hydroxyapatite for efficient catalytic activity towards 4-nitrophenol reduction, Res. Chem. Intermediat. 44 (2) (2018) 1189-1208, **http://dx.doi.org/10.1007/s11164-017-3161-7**.

[43]   M. Chernykh, N. Mikheeva, V. Zaikovskii, G. Mamontov, Influence of the Ag content on the activity of Ag/CeO2 catalysts in the reduction of 4-nitrophenol at room temperature and atmospheric pressure, Kinet. Catal. 61 (5) (2020) 794-800, **http://dx.doi.org/10.1134/S002315842005002X**.